REPORT DOCUMENTATION PAGE

Form Approved
OMB No. 0704-0188

1. REPORT DATE *(DD-MM-YYYY)*	2. REPORT TYPE	3. DATES COVERED *(From - To)*
25-02-2019	Final Technical Report	09/01/2015 - 11/30/2018

4. TITLE AND SUBTITLE
Persistent Maritime Quantum Key Distribution

5a. CONTRACT NUMBER

5b. GRANT NUMBER
N00014-15-1-2393

5c. PROGRAM ELEMENT NUMBER

6. AUTHOR(S)
Huang, Yuping
Yu, Ting
Martini, Rainer

5d. PROJECT NUMBER

5e. TASK NUMBER

5f. WORK UNIT NUMBER

7. PERFORMING ORGANIZATION NAME(S) AND ADDRESS(ES)
Stevens Institute of Technology
One Castle Point on Hudson
Hoboken, NJ 07030-5991

8. PERFORMING ORGANIZATION REPORT NUMBER

9. SPONSORING/MONITORING AGENCY NAME(S) AND ADDRESS(ES)
Office of Naval Research
875 N. Randolph Street Suite 1425
Arlington, VA 22203-1995

10. SPONSOR/MONITOR'S ACRONYM(S)
ONR

11. SPONSOR/MONITOR'S REPORT NUMBER(S)

12. DISTRIBUTION/AVAILABILITY STATEMENT
Approved for Public Release; Distribution is Unlimited

13. SUPPLEMENTARY NOTES

14. ABSTRACT

This report summarizes the findings of the whole project, whose purpose is to identify and develop suitable techniques for quantum secure communications over maritime environment. The focus is on overcoming the absorption, multiscattering, turbulence, and background radiation that commonly exist in maritime atmospheres. To this end, this project executed experimental and theoretical research in the following three areas: comparison analysis of wavelengths for maritime quantum communications using a laboratory testbed; theoretical studies on entanglement transmission and optimal coding thereupon; experimental demonstration of entanglement generation and detection in the optimized modes. This report provides technical details in those three research areas, which aggregately point to a viable wavelength channel for maritime quantum communications around 3.95 micron. Comparing with existing wavelength choices in the visible or near infrared spectra, this new wavelength offers unmatched advantages in overcoming multiscattering, turbulence, and heat scintillation.

15. SUBJECT TERMS
quantum communications; free space optical links; quantum optimal coding; upconversion detection; entanglement generation; parametric downconversion.

16. SECURITY CLASSIFICATION OF:			17. LIMITATION OF ABSTRACT	18. NUMBER OF PAGES	19a. NAME OF RESPONSIBLE PERSON
a. REPORT	b. ABSTRACT	c. THIS PAGE			Yuping Huang
U	U	U	UU	30	19b. TELEPHONE NUMBER *(Include area code)* 201-216-5709

INSTRUCTIONS FOR COMPLETING SF 298

1. REPORT DATE. Full publication date, including day, month, if available. Must cite at least the year and be Year 2000 compliant, e.g. 30-06-1998; xx-06-1998; xx-xx-1998.

2. REPORT TYPE. State the type of report, such as final, technical, interim, memorandum, master's thesis, progress, quarterly, research, special, group study, etc.

3. DATES COVERED. Indicate the time during which the work was performed and the report was written, e.g., Jun 1997 - Jun 1998; 1-10 Jun 1996; May - Nov 1998; Nov 1998.

4. TITLE. Enter title and subtitle with volume number and part number, if applicable. On classified documents, enter the title classification in parentheses.

5a. CONTRACT NUMBER. Enter all contract numbers as they appear in the report, e.g. F33615-86-C-5169.

5b. GRANT NUMBER. Enter all grant numbers as they appear in the report, e.g. AFOSR-82-1234.

5c. PROGRAM ELEMENT NUMBER. Enter all program element numbers as they appear in the report, e.g. 61101A.

5d. PROJECT NUMBER. Enter all project numbers as they appear in the report, e.g. 1F665702D1257; ILIR.

5e. TASK NUMBER. Enter all task numbers as they appear in the report, e.g. 05; RF0330201; T4112.

5f. WORK UNIT NUMBER. Enter all work unit numbers as they appear in the report, e.g. 001; AFAPL30480105.

6. AUTHOR(S). Enter name(s) of person(s) responsible for writing the report, performing the research, or credited with the content of the report. The form of entry is the last name, first name, middle initial, and additional qualifiers separated by commas, e.g. Smith, Richard, J, Jr.

7. PERFORMING ORGANIZATION NAME(S) AND ADDRESS(ES). Self-explanatory.

8. PERFORMING ORGANIZATION REPORT NUMBER. Enter all unique alphanumeric report numbers assigned by the performing organization, e.g. BRL-1234; AFWL-TR-85-4017-Vol-21-PT-2.

9. SPONSORING/MONITORING AGENCY NAME(S) AND ADDRESS(ES). Enter the name and address of the organization(s) financially responsible for and monitoring the work.

10. SPONSOR/MONITOR'S ACRONYM(S). Enter, if available, e.g. BRL, ARDEC, NADC.

11. SPONSOR/MONITOR'S REPORT NUMBER(S). Enter report number as assigned by the sponsoring/ monitoring agency, if available, e.g. BRL-TR-829; -215.

12. DISTRIBUTION/AVAILABILITY STATEMENT. Use agency-mandated availability statements to indicate the public availability or distribution limitations of the report. If additional limitations/ restrictions or special markings are indicated, follow agency authorization procedures, e.g. RD/FRD, PROPIN, ITAR, etc. Include copyright information.

13. SUPPLEMENTARY NOTES. Enter information not included elsewhere such as: prepared in cooperation with; translation of; report supersedes; old edition number, etc.

14. ABSTRACT. A brief (approximately 200 words) factual summary of the most significant information.

15. SUBJECT TERMS. Key words or phrases identifying major concepts in the report.

16. SECURITY CLASSIFICATION. Enter security classification in accordance with security classification regulations, e.g. U, C, S, etc. If this form contains classified information, stamp classification level on the top and bottom of this page.

17. LIMITATION OF ABSTRACT. This block must be completed to assign a distribution limitation to the abstract. Enter UU (Unclassified Unlimited) or SAR (Same as Report). An entry in this block is necessary if the abstract is to be limited.

Persistent Maritime Quantum Key Distribution

Grant # N000141512393

Final Technical Report

PIs: Yuping Huang (Yuping.Huang@stevens.edu)
Rainer Martini (Rainer.Martini@stevens.edu)
Ting Yu (Ting.Yu@stevens.edu)

1. Project Objectives and Main Findings

The objective of this project is to overcome the challenges facing free-space QKD in the highly dynamic maritime environment, by developing a new platform for free-space QKD that is persistent under adversary weather conditions while also achieving high-photon efficiency. Distinct from existing studies, we deploy single photons at around 4 microns, which corresponds to the optimal, perhaps the only, wavelength band that survives simultaneously absorption, scattering, and in-coupling of background radiation under various weather conditions. By developing advanced encoding and decoding protocols for photonic qudits in this band, we are working to establish a practical maritime QKD platform operable even when the visibility is low.

To this end, our effort focuses on the following four major areas.
The first is to experimentally characterize and theoretically model maritime QKD channels, including important parameters such as absorptive loss, scattering, chromatic dispersion, polarization dispersion, and background noise. For a comparative analysis, we construct a multi-wavelength transmission testing system and monitor transmission of multiple wavelengths. Parallel to the experimental effort, we develop and modify existing theoretical models to incorporate the new findings, allowing for more accurate simulation of the for maritimeQKD relevant parameters.

Second, we develop quantum optical arbitrary waveform measurement (QOAWM), a technique capable of fully-vectorial qantum-state tomography (QST) of photonic qudits in the mid-infrared regime (e.g., ~4 microns). Contrary to existing methods, our QOAWM employs quantum frequency conversion (QFC) in a nonlinear waveguide which converts an incident photon at ~4 micron to near 630 nm. Uniquely, we use mode-tailored pump pulses to selectively convert the incident photons in spectrally and temporally overlapping pulses according to their amplitude and phase profiles. As this function is achieved through a single pass through a conventional QFC waveguide, the quantum signals experience minimal loss and in-coupling of noise. Detecting the converted photons can allow one to measure the mid-infrared photonic qudits in any single mode or an arbitrary superposition of the modes. Our approach presents some enabling advantages for maritime QKD. First, it allows for coding quantum information in overlapping time-frequency modes, as opposed to the usual pulse-position coding where the time bins must be sufficiently spaced to avoid cross talk. This opens a door to QKD exploiting the maximum useable phase space (given by the time-bandwidth product of the optical signals in our case). Second, the use of up-conversion detection boosts detection efficiency for the mid-infrared single photons while suppressing the dark counts through the use of mature Si-based avalanche-photodiode (APD) technology.

Third, in our method only those photons in the time-frequency mode of interests is converted and subsequently detected. All photons in other modes are not converted and will not reach the APD's.

This unique feature helps to clean up the maritime-QKD channels which are swarmed by blackbody radiation photons spreading over all modes. By rejecting all modes but one the quantum signal resides, nearly all background photons will not contribute to detected noise, giving rise to the maximum protection of our quantum channel. Fourth, our method has the built-in capable of compensating group-velocity dispersion, implemented without need for external dispersion compensation. This could provide a viable, minimum-cost solution to overcome chromatic dispersion for free-space maritime channels. Finally, it allows for high-speed QKD at a clock rate well above GHz, the latter set by the current single-photon detection techniques. This is because for QOAWM the detection timing jitter is determined by the pump pulses driving QFC, which can be ~picosecond or even less.

Third, we develop a lossless photon shaping technique for generating photonic qudits in overlapping-pulse modes. Existing methods for creating mode-shaped photons have relied on applying phase or amplitude modulation directly on the priori-created single-photon pulses. They thus suffer from significant transmission and modulation losses, and, depending on the devices used, injection of in-band quantum noise. In contrast, we employ an indirect modulation method to create mid-infrared photonic qudits in fine tailored time-frequency modes, where pump pulses near 1550 nm are created in appropriate amplitude and phase profiles using a cavity-based frequency comb source and an optical arbitrary waveform modulation (OAWG) device. With appropriate frequency filtering and time gating, photons can be created at high speed while maintain a high quantum state purity. Such a photon source satisfy simultaneously all operational criteria for practical applications: room-temperature, scalable, versatile, and compact.

Fourth, we investigate the influence of environmental noises on high-dimensional QKD under atmospheric weather conditions, including clear maritime, turbulence, and various levels of rain and fog. Despite increased activity and heightened attention, the implementation of a QKD scheme in a realistic maritime environment is largely lacking and our understanding of quantum communication of a quantum key system under the influence of multiple real-world noise is rather primitive. Unlike QKD in optical fiber where the loss and decoherence mechanism is well understood, the quantum dynamics of photonic signals over long maritime distance (e.g, 30 km) is rather subtle and complex. Our first priority is to establish a realistic noise model for the maritime environmental noises with different spectra. For instance, we use classical white noise to simulate background radiation, random fluctuation and turbulence influence. For low frequency noise generated by random vibration and sea-surface noise, colored noises must be taken into account in order to provide an accurate model for the decoherence process. Based on our multiplicative noise model, we study robust qudit-QKD taking into account of the noise properties of optical transmission under various maritime weather conditions. Through mathematical model and numerical simulations, we can subsequently identify optimal wavelength of transmission signals against the decoherence effects of atmosphere on quantum communication channel.

2. Educational Outcomes

2 PhD students and 2 postdoc have been trained in areas of experimental quantum optics.
1 PhD students have been trained on the theory of quantum stochastic processes, modeling the propagation of quantum signals over dynamic, complex atmospheres.
3 PhD students have been trained on experimental characterization of optical transmission in simulated environment (fog tubs, heat scintillations, ...).

3. Results Dissemination

1. "Direct Generation and Detection of Quantum Correlated Photons with 3.2 um Wavelength" Spacing YMSua, H Fan, A Shahverdi, JY Chen, YP Huang Scientific reports 7 (1), 17494 (2017);

2. "Quantum Parametric Mode Sorting: Beating the Time-Frequency Filtering," A Shahverdi, YM Sua, LTumeh, YP Huang Scientific Reports 7, 6495 (2017).

3: "Mode selective up-conversion detection for LIDAR applications," Amin Shahverdi, Yong Meng Sua, Ivan Dickson, Malvika Garikapati, and Yu-Ping Huang, Optics Express Vol. 26, Issue 12, pp. 15914-15923 (2018).

4: "Ultra-wideband and high-gain parametric amplification in telecom wavelengths with an optimally modematched PPLN waveguide," Yong Meng Sua, Jia-Yang Chen, and Yu-Ping Huang, Optics Letters Vol. 43, Issue 12, pp. 2965-2968 (2018)

5. "Selective Detection of Picosecond Overlapping Quantum Modes" A Shahverdi, M Sua, YP Huang LaserScience, JW4A. 27 (2017);

6. "Quantum Airy Photons," S Maruca, YM Sua, A Shahverdi, YP Huang, Journal of Physics B: Atomic, Molecular and Optical Physics 51, 175501 (2018).

7: "Weather-proof Quantum Communications," YM Sua, H Fan, A Shahverdi, R Martini, Y Huang Frontiers in Optics, FM2D. 3

8: "Comparison of mid- and near-infrared link losses in simulated scattering and turbulent environment." Zhang, D., Kumar, P., Bu, T. & Martini, R. PTh3D.5 (Optical Society of America, 2017).

9: "Mode-Selective Image Upconversion," Santosh Kumar, He Zhang, Stephanie Maruca, and Yu-Ping Huang, Optics Letters Vol. 44, Issue 1, pp. 98-101 (2019).

10: "Ultra-wideband parametric amplification in telecom wavelengths with an optimally mode-matched PPLN waveguide," Yong Meng Sua, Jia-Yang Chen, Yu-Ping Huang, Optics Letters Vol. 43, Issue 12, pp. 2965-2968 (2018).

11: "Noise tolerant LIDAR via mode selective up-conversion detection," Amin Shahverdi, Yong Meng Sua, Ivan Dickson, Malvika Garikapati, and Yu-Ping Huang, Frontier in Optics, paper JTu3A.8.

4. Technical Details:

4.A Comparison analysis of wavelengths

In this part, we have performed extensive experimental studies, along with some theoretical modeling, on the transmission of near-IR and mid-IR wavelengths through various types of

atmosphere that simulate that of maritime environment. Much stronger losses are measured for a near-infrared link compared to a mid-infrared propagating through a simulated fog in turbulent media. The turbulence is additional quantified through direct beam measurement at both wavelengths.

I.1. Introduction

As proposed, the authors investigate the influence of simulated maritime atmospheric conditions on the propagation parameters in the near-infrared (NIR) in comparison to the mid-infrared (MIR) spectral region including scattering from aerosol particles, turbulence and to our knowledge for the first time the combined effect of scattering from aerosol under in turbulent media. To establish a realistic noise model we use the in-lab enclosure with increased scattering and turbulence environment, yet generate an environment comparable to long distance maritime environment. It should be especially pointed out that we have observed a strong dependence on wind speed as well as a new phenomena in the combination of scattering and turbulence that has an important impact on the resilience of free-space communication link in an environment where both aerosol scattering and turbulence are present.

Most experimental and theoretical research has been either focused on scattering losses in the propagation link [1-3] or on turbulence losses in the link [4]. It has been the assumption that both losses can be handled separately and the total extinction coefficient is the sum of the separate losses. In contrast to previous experiments, the authors presented here a more realistic simulation setup where the losses in a controlled scattering and turbulence environment are affecting the propagation of links with different wavelength at the same time – which allows for the observation of relative changes. Overall losses for scattering and turbulence as well as direct measurement of the beam parameters for turbulence alone have been measured and the link performance compared, demonstrating again the much higher resilience of a mid-infrared (MIR) link (4328nm) compared to a near-infrared (NIR) link (1550nm).

I.2. Experimental setup

Fig. 1 shows schematically and not to scale the setup used for the measurement: a MIR link operating at 4328nm and a NIR link operating at 1550nm are modulated by separate frequencies (through a chopper), indidually focused and combined to have the same beam path. They then propagate through a 1.2m long tube enclosure, which leads to a separate enclosure containing a remotely controlled heat plate, which enable us to initiate different degree of turbulence, thus create correspondent scintillation. The tube is connected to a water-based fog generator, entrance and exit flow control (not shown) allow for controlled filling and evacuation of the connected spaces with fog to realize different scattering scenarios, i.e. fog concentration and hence different levels of visibility. A monitoring system is integrated in the enclosure to measure temperature and wind speed, etc, (shown in Fig.2), to ensure constant environment conditions between measurements.

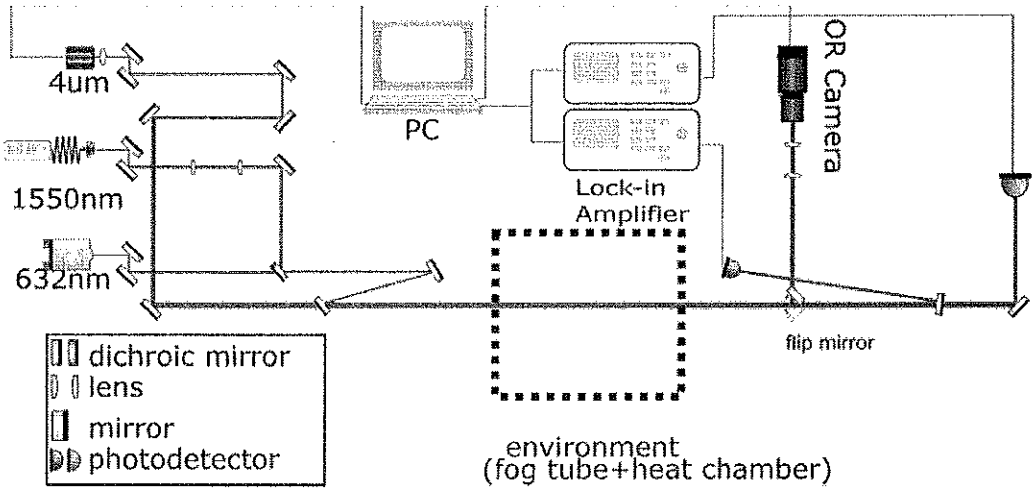

Fig.1 Experimental setup.

After propagation through the simulated scattering and turbulence area, the two links beams are separated using wavelength selective beam splitters, and their power level detected. The losses in each link are measured by two lock-in amplifiers to minimize crosstalk and allow for a dynamical range of 5 orders of magnitude, i.e. compare the losses of the different wavelengths even under heavily scattering scenarios. In addition, the individual beam properties (both position and size) can be monitored in real time using an in house designed optical readout (OR) camera, which is able to detect and analyze the beam profile for wavelengths ranging from the visible into the THz spectrum [5] – and hence allows us a direct analysis of the beam degradation.

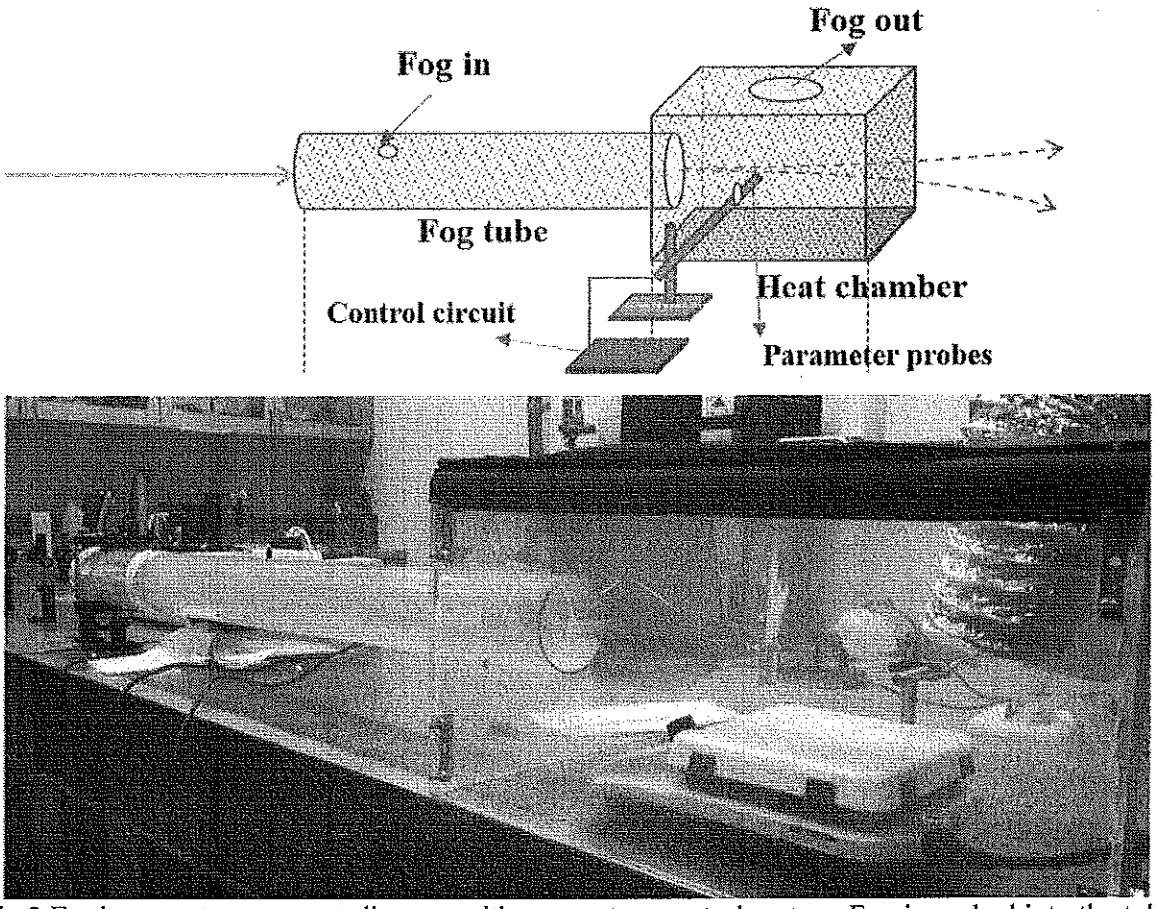

Fig.2 Environment component diagram with parameters control system. Fog is pushed into the tube and flow though the tube and chamber and out to the vent. The parameter control system can control the temperature of the heat plate and vent wind speed, and record temperature, pressure, and vent fan speed.

I. 3. Scattering power loss analysis

In a first of experiments the scattering losses for each link are determined at room-temperature and without any additional turbulence present. During the experiment, the enclosure is first filled with fog resulting in complete loss of transmission (~-40 dB losses), which simulates the situation for FSO links in strong fog condition over medium distances (~1km) or under medium fog condition in long distances. Slow and controlled evacuation of the fog allows then to monitor the recovery of the links whereby the MIR link recovers much faster than the NIR link. As soon as both links are detectable the relative losses can be easily monitored and compared. The inset of fig. 3 shows exemplary such a recovery for both links, while the main figure shows the relative losses for NIR link in dB plotted against the corresponding MIR losses for a typical measurement obtained over several minutes. Alone from the scale it is obvious, that the NIR link experiences much stronger losses. At the minimum detectable level of the NIR link with 40dB losses the MIR link power is only reduced by 7.5dB. This is attributed to the well-documented fact that the longer wavelength is much less affected by aerosol particle smaller than its wavelength. Fitting the data with a linear regression algorithm allows then to quantify the difference in extinction coefficient for the MIR and NIR laser – in this experiment the NIR scattering extinction coefficient appeared to be nearly 5.5 times higher compared

to the MIR link, hence showcasing the resilience of the MIR link.

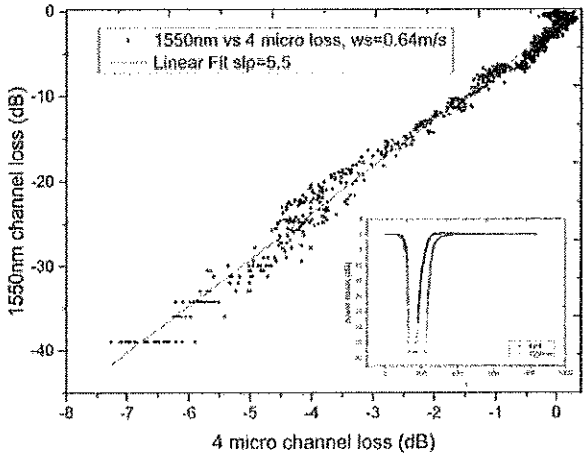

Fig.3 Power loss comparison between 1550nm and 4μm with scattering material: comparing the two links against each other, at wind speed(ws) = 0.64m/s under the room temperature of 21°C, The inset shows power variation of MIR and NIR over time, both links show about 0 to -40dB dynamic range, but NIR show a much slower recovery.

While repeating this experiments multiple times it was observed that the speed of emptying the enclosure form the fog – which is further to referred to as the wind-speed had a strong influence on the scattering rate – and affected especially the ratio between the NIR and MIR losses. To control this parameter and hence allows for consistent data the speed of ventilation fan was controlled using a PID loop, which resulted in much more stable measurement. The data shown above in Fig. 3 were obtained at a wind speed of 0.64m/s for example. It was found that with increasing wind speed the losses for the NIR link increased strongly compared to the losses in the MIR link. Using the same methodology as described above, pure scattering experiments were performed at three different wind speed, and the slopes of the relative power loss comparisons determined – which represent the extinction coefficient ratios. Fig. 4 shows those plotted against the wind speed, whereby the second data point refers to the measurement shown in Fig. 3. The error of the data points were determined from the linear fit algorithm – in all cases a very good linear fit was obtained.

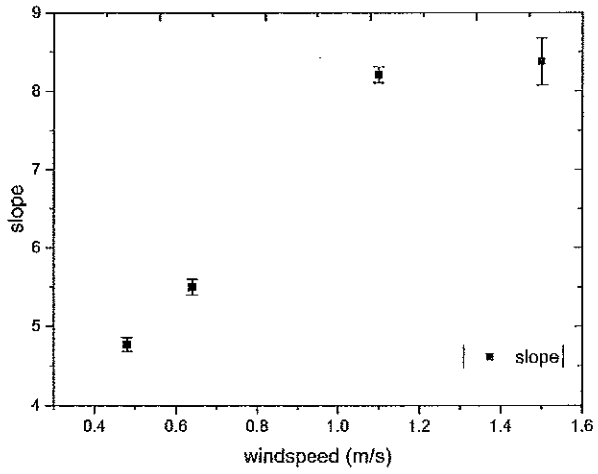

Fig.4 Slope of power losses varies due to wind speed change.

It is obvious that the NIR link experience far stronger losses with increasing wind speeds until the effect seems to saturate at wind speeds above 1.3 m/s. However, the increased error bar demonstrates much less accurate data extraction as the fog is evacuated out of the enclosure very fast. However, the slope varies from 4.8 at a wind speed of ~0.48m/s to 8.5 at the highest wind speed of 1.5m/s – which is nearly twice as high. We attribute this observation to movements of scattering material which increases there the relative scattering efficiency especially for shorter wavelength – yet further measurements are performed to clarify and verify this result.

I. 4. Turbulence analysis based on camera tracking and Kolmogorov theory

In contrast to the scattering losses which are typically only described and predicted using the deterministic developed Kruse-Mie approximation, the theoretical description of turbulence is much more developed. Kolmogorov developed a theory of turbulence that the atmosphere around the optical beam path can be seen as viscous eddies, which then would create local variation in the index of refraction – which then in turn leads to beam wander and intensity fluctuations. The index of refraction structure constant (C_N^2) of the atmosphere is frequently used to quantify the effect of such eddies on beam propagation, which can be calculated from the autocorrelation and covariance of its power spectrum. Generally, the turbulence is "weak" with values of C_N^2 around $10^{-17}\ m^{-2/3}$ or less, while it is "strong" with C_N^2 up to $10^{-13}\ m^{-2/3}$ or more, for typically atmospheric condition one expects a C_N^2 value of $10^{-14}\ m^{-2/3}$ near ground. The Scintillation index (or Rytov variance) characterizes then how the beam propagation is effected and it is calculated from the covariance function of irradiance, shown as Eq.(1).

$$\sigma_R^2 = 1.23 C_n^2 k^{7/6} \left[(L_2 + L_3)^{11/6} - (L_3)^{11/6}\right] \qquad (1)$$

Where $\alpha = 11/3$ for Kolmogorov spectrum and the lengths (propagation length before, in the turbulent area, and after it) are shown in figure 27. For long-distance propagation, we assume that the whole propagation length experiences turbulent air movement (i.e. $L_2 \approx L$, $L_1 \approx 0$, $L_3 \approx 0$, and L is the total optical beam path) so that the formula simplifies to $\sigma_R^2 = 1.23 C_n^2 k^{7/6} L^{11/6}$.

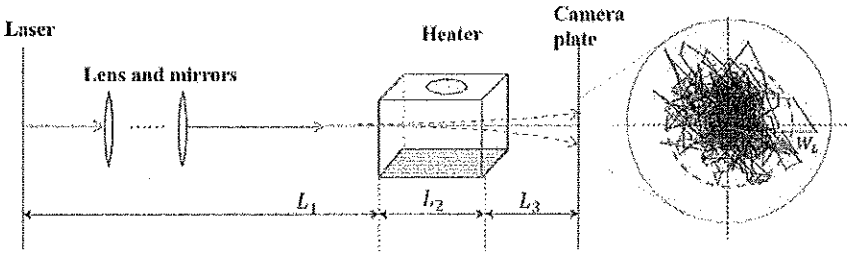

Fig.5: The structure diagram for beam propagation with turbulence only and the random walk captured by the camera.

At the same time the Rytov variance is also the function that determines the average beam wander (random walk of the beam center). Hence we can derive a formulation of the beam wander depending on C_N^2 (Eq.(2)):

$$W_L^2 - W^2 = 1.63 * 2L^{16/5} * k^{2/5} [1.23C_n^2]^{6/5} \quad (2)$$

Whereby W_L is the effective measured increased beam width (based on the random beam wander) if measured over a long time period (as shown in Figure 5), and W_0 is the original beam width. Based on the analysis of the beam wander videos, we find that the beam wander is approximately obey Gaussian distribution - especially for weak turbulence conditions.

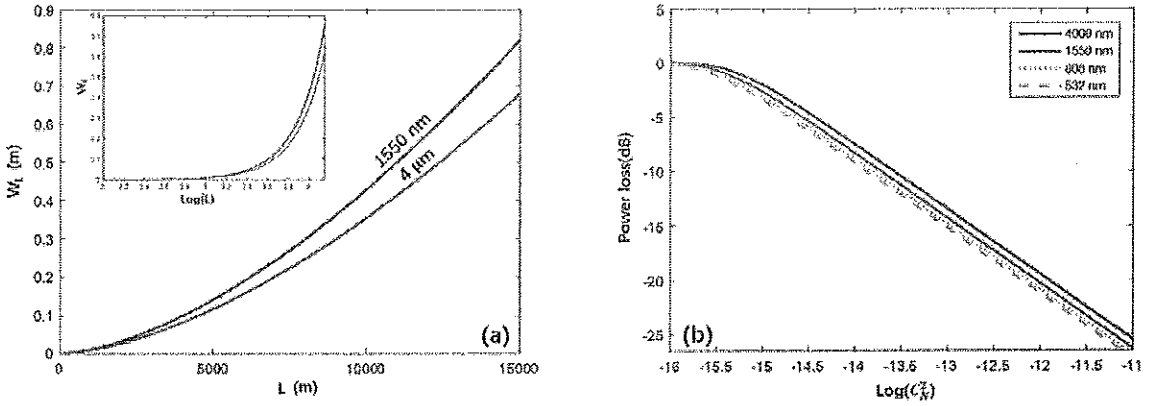

Fig.6 (a)The beam wander W_L with respect to L (1m ~ 15 km) with $C_n^2 = 10^{-14}\, m^{-2/3}$. And the inset is W_L vs log(L). (b)Power loss in dB for the beam with C_n^2 in 10^{-16}~$10^{-11}\, m^{-2/3}$, L = 15 km.

To explain the expectation of loss variation for different wavelengths several simulations were performed, which are shown in Fig. 6. Figure 6 (a) shows the dependency on the final beam width $\boldsymbol{W_L}$ on the propagation length L for an average value of ($\mathbf{10^{-14}\, m^{-2/3}}$) for $\boldsymbol{C_n^2}$. As expected $\boldsymbol{W_L}$ increases with distance and the inset shows the the same plotted against the logarithms of the distance – to showcase the increase better. For the longest distance L = 15 km and $\boldsymbol{C_n^2 = 10^{-14}\, m^{-2/3}}$, the NIR beam width expands to $\boldsymbol{W_L}$=0.81 m for a 1550 nm laser, while the MIR link will stay a little smaller ($\boldsymbol{W_L}$=0.67 m for the MIR link). Based on this relationship the losses due to scintillation alone can be estimated assuming the same detector size – which is shown in Figure 6 (b). In the simulation for long distance propagation, the aperture of the receiving optics is set to 5cm. No or only very small power losses are observed at $\boldsymbol{C_n^2 = 10^{-16}\, m^{-2/3}}$, as the radius $\boldsymbol{W_L}$ is of the same order or smaller than the receiving optics size. Yet with increasing turbulence and hence $\boldsymbol{C_n^2}$, the radius of the beam wander becomes larger, and thus power loss appear. To showcase the effect for different

wavelengths, four different wavelength were selected and plotted in different colors. It can be seen that the power losses are smaller for larger wavelengths (i.e. a MIR will have less turbulence related losses compared to a NIR – due to its smaller beam wander) – yet the effect seems to be roughly constant and not depending on the strength of the turbulence. Thereby based on pure Kolmogorov scattering theory the MIR has a small advantage – but nno remarkable superiority in the turbulence-only case for communication.

To actually analyze and quantify the effect of the turbulence on the beam propagation (and compare it to the theoretical predictions), the beam spot of each link has been recorded over an extended period of time in separate measurements. By using an optically readout approach, identical setups and recording equipment was applied to record the beam spot for the NIR laser link as well as the MIR laser link under the same turbulence condition, yet without any fog present. Evaluation of a 3 minutes from a recorded movie (at 30 frame per seconds) allows for measurement of beam spot size and position and thereby direct observation of beam wander and fluctuation of beam size at each frame. Aside of a direct comparison of the effect on the two different links, it allows us also to quantify the turbulence directly based on the measured beam spot parameter.

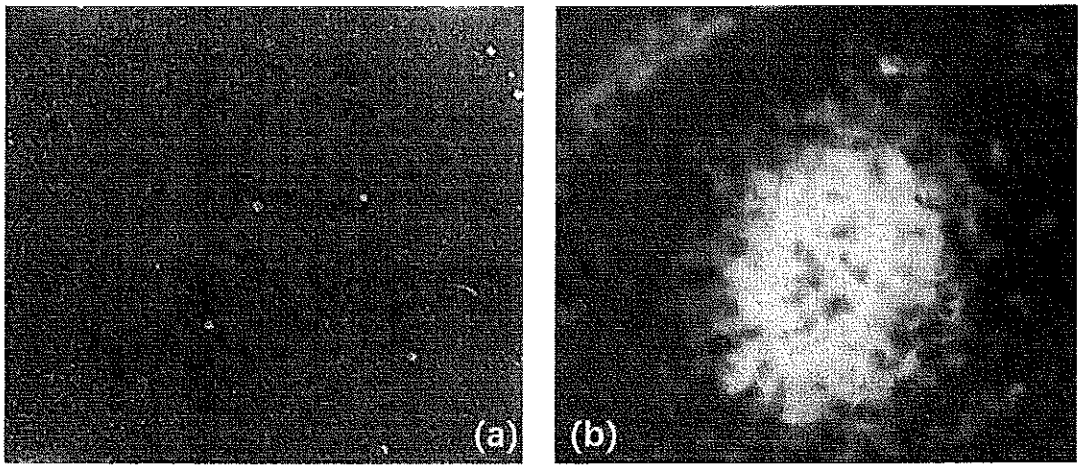

Fig. 8 (a) TLC Imaged captured by CMOS color camera and (b)Processed image showing the relative intensity of laser spot

Tremendous effort was spent on establishing an image capture and analysis program using Python scripts and QT for user interface. In the final version the camera was able to capture each frame from the OR camera system (left), post process the image to identify size and convert it to a relative intensity map which then allowed for determination of laser spot position and size.

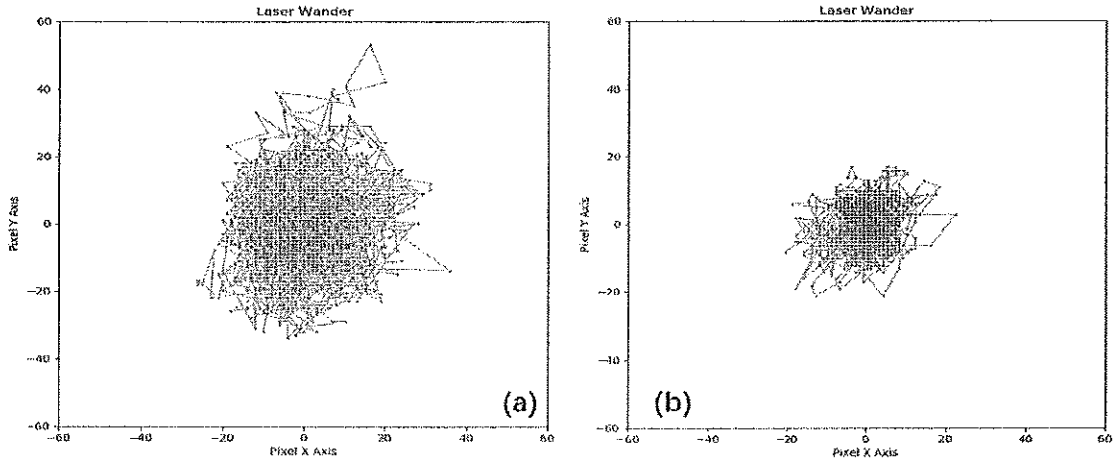

Fig. 9 (a) 1550nm wander @80C air temperature (b) 4μm wander @80C air temperature

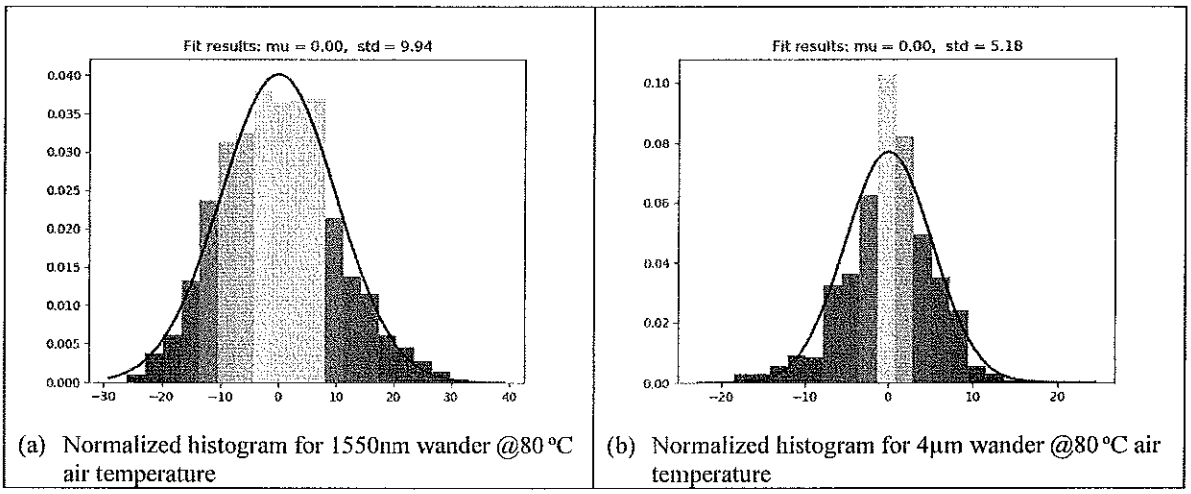

(a) Normalized histogram for 1550nm wander @80 °C air temperature

(b) Normalized histogram for 4μm wander @80 °C air temperature

Fig.10 Normalized histogram for (a) 1550nm and (b) 4μm beam wander @80°C air temperature

Fig. 9 shows exemplary beam wander plots (i.e. the extracted movement of the center of the laser spot) for the NIR and the MIR laser under strong turbulence conditions (air temperature of 80 degree Celsius) with the same spatial scale. It is obvious that the NIR beam experiences much stronger beam wander compared to the MIR link. To quantify these movements better a histogram analysis is used and shown in Fig. 10. Again the stronger beamwander in the NIR laser link is obvious, leading to a bigger average beam width and hence increased losses in the link compared to the MIR link. Additional measurements for other turbulence conditions and dependency on windspeed are performed right now, which will then allow to quantify the losses differences for different wavelengths and hence confirm or reject the predictions from the Kolmogorov scattering theory.

I. 5. Simultaneous scattering and turbulence power loss analysis

While the effect of scattering has been separately analyzed and the turbulence losses are examined independently as well, the authors now add turbulence to the propagation path through the hot air stemming from as hot surface. It is particular interesting to examine the relative losses caused by scattering and turbulence, i.e. fog is being present and becoming part of the turbulent air movement

in the enclosure. The temperature is monitored at the same height as the optical path and documented. Based on the previously mentioned assumption that scattering losses and turbulence losses are independent of each other, one expected only an additional loss in both links (slightly stronger in the NIR link due to the stronger beam wander), yet those losses would be only due to turbulence and hence not scale with the scatter concentration. In other words, one could conclude that repeating the original methodology what produce parallel datasets with identical slopes showcasing that the losses relying on scatter concentration remain the same and are not affected by turbulence.

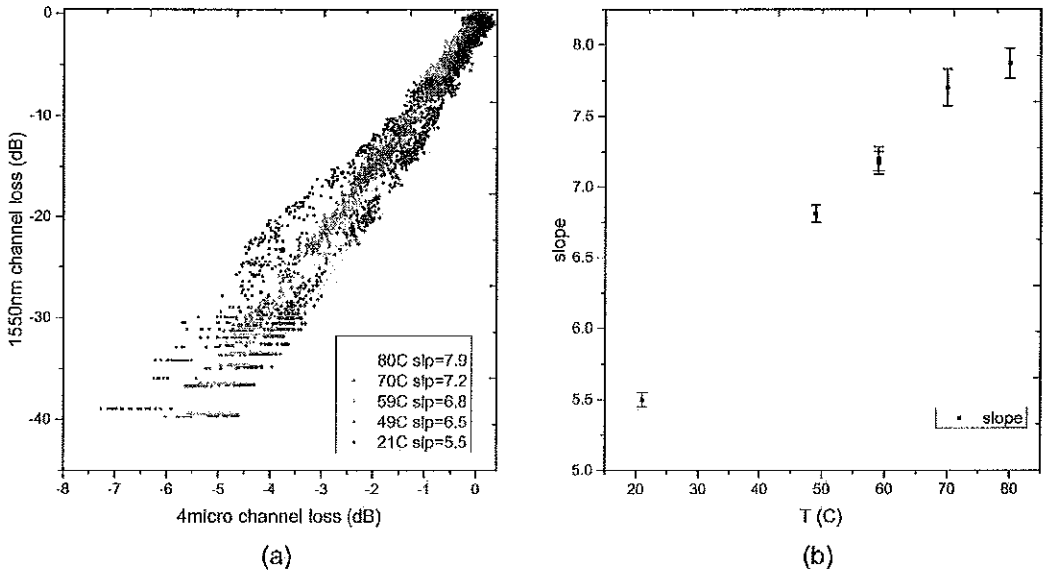

Fig.112 Power loss comparison between 1550nm and 4μm at different enclosure temperature at ws=0.64m/s, (b) shows slopes of the linear fit to the power losses in each temperature

However, adding the fog to the system while turbulence is present, the losses for the NIR link increase dramatically, and the NIR link broke down much sooner. As with speed before the losses scales with the amount of aerosol particle present (i.e. fog) present. Shown in Fig.11 (a), at lower fog concentration, MIR experiences 0 to -1dB loss, while the NIR experiences 0 to -10dB, wich would be in line with previous observation. However, as fog concentration increases, the experiment results clearly contradicts the expectation, in the worst case scenario, when MIR experiences only a 5dB loss while the NIR link drops out again 40bB losses – at lower turbulence the NIR losses reached 40dB at MIR loss values of 7dB. This variation indicates that under turbulent conditions, the scattering seemed to be more efficient for shorter wavelengths. Figure 11 (b) show the clearly the performance difference: Deducing again the slopes (representing the exponential losses of the MIR in relation to the NIR link) the losses for the NIR increase from 5.5 to 7.9 in relation to the MIR link, showcasing an even much more pronounced resilience of a MIR link in the presence of turbulence and fog.

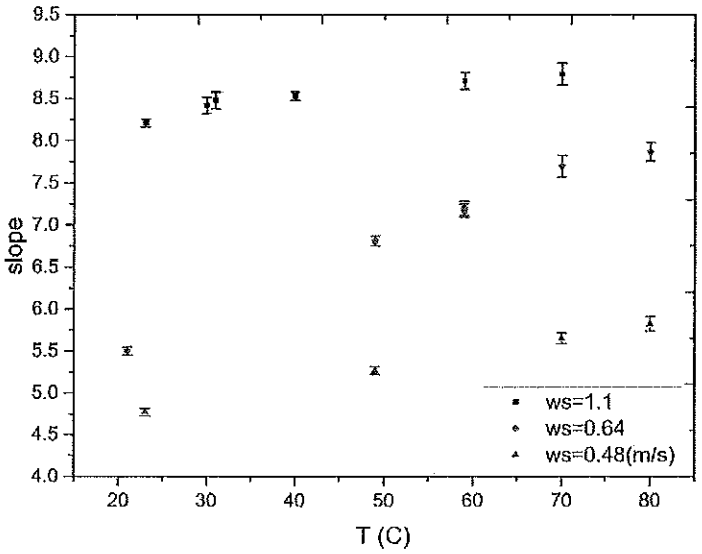

Fig. 12 Slope variation in different temperatures and different wind speeds

Additionally, when the temperature of the enclosure stays roughly the same, changing wind speed, thusly changes the behavior of the fog also results in different comparison of the two said wavelengths. Figure 12 shows the plot of different extinction coefficient ratios in different enclosure temperatures under different wind speed. In each chosen wind speed, the tendency holds true, that the MIR link is more resilient as temperature increases. However, the advantages seemed to be strongest at medium wind speed and taper off for low or higher wind speed. However – it should be pointed out that this are only new results and more measurements and data analysis is needed.

When looking at one chosen temperature, for instance as Fig.3 shows, NIR again is outperformed by MIR link, and the ratio increases as the wind speed increases, while shown in Fig.4, at 70°C, the ratio difference narrowed, from 3.4 to 2.5. Due to wind speed change, the fog flows through the enclosure at a different rate and pattern, while the microscopic behavior of the turbulent eddies shows different uniformity. Thus shows the different influence of the extinction coefficient ratio. But it should be pointed out that a quantitative tendency of the wind speed influence needs to be further established.

It should be also clearly pointed out that the presence of very strong turbulence seemed to increase the scattering efficiency for a given fog concentration, and it particular for NIR links. This observation could only made in our setup where losses at two different wavelengths are measured and compared with each other. The unique experimental setup here allowed clearly distinguishing the effect of scattering, and turbulence with scattering in turbulent media. In addition, the ability to separate the response by monitoring the optical link properties in different wavelength region allows for the first time to identify an increase in scattering efficiency for smaller aerosol particles under the presence of turbulence. To clarify the result: under the same concentration of aerosol scatters present (as deduced by the same losses in the MIR link – for example -4.5dB) the presence of turbulence (fast moving air) leads to a more than doubling of losses for the NIR link (to be more precise from -25dB without turbulence to over -40dB). Hence increasing the air movement (turbulence) will further increase these losses clearly identifying the presence of turbulence as the reason for the increased losses in the NIR link – all while the MIR link largely remained unaltered. A first attempt of explanation can be made assuming that the smaller aerosol particles are actually moving within the

link area – and hence create an effective scattering area bigger than the aerosol particle itself. These particle movements will be much less for larger particle – and hence a link operating at a longer wavelength will be less impacted. However, more comprehensive research on microscopic behavior effect is needed before a more conclusive theory can be formed.

Nonetheless, these results are in striking contrast to the typical link budget formula, where losses attributed to turbulence and scattering are independently calculated and simply added. And the magnitude of the changes observed (more than doubling the losses in the NIR link) clearly underlines the importance of this newly discovered effect.

I.6. Conclusion and Outlook

The unique setup built within this grant has displayed again clearly the higher resilience of a MIR link against low visibility conditions as indicated in the grant proposal. Yet it has delivered also two important new results, which clearly needs further measurements and evaluation:

1. Calculate the NIR losses due to aerosol scattering increase in the presence of a turbulent media compared to the losses measured in a MIR link and contradict the common assumption that scattering losses can be independent from the turbulence losses. In specific, the losses for NIR links are clearly underestimated if taken only aerosol concentration into account and not including the media flow. However, a new theory has to be developed to allow further explanation of this effect.
2. Measure the beam wander due to turbulence separately for MIR and NIR links and compare it with the theoretical predictions. If needed a new model has to be developed – otherwise the link losses even in a scatter free link can be measured and compared with the measured ones.
3. In comparison the MIR link experienced also less loss compared to the NIR under different wind speed situations. This also needs further measurements and needs as well clear separations from the two above mentioned observations.

In any case – all this new observation are clearly very relevant in estimating the losses in free-space optical communications – and the observed cross talking between scattering and turbulence as well as the dependency on wind-speed have been to our knowledge not reported in the literature. Yet further experiment and modeling are needed to deepen our understanding the microscopic reason of the discussed behavior of MIR and NIR link in scattering and turbulent channel.

References

[1] P. Corrigan, E.A. Whittaker, E.A. Whittaker, and C. Bethea, "Quantum cascade lasers and the Kruse model in free space optical communication", Optics Express 17, 4355-4359 (2009).

[2] A. Rashed and M. El-Halawany, "Transmission Characteristics Evaluation Under Bad Weather Conditions in Optical Wireless Links with Different Optical Transmission Windows", Wireless Pers Commun 71, p. 1577–1595 (2013).

[3] X. Wu, H. Wang, and B. Song, "Measurement of fog and haze extinction characteristics and availability evaluation of free space optical link under the sea surface environment", Applied Optics 54 (5), 1015-26 (2015).

[4] See for example I. Toselli, B Agrawal, and S. Restaino "Gaussian beam propagation in maritime atmospheric turbulence: long term beam spread and beam wander analysis", Free-Space Laser Communications X, Proc. of SPIE Vol. 7814, 78140R (2010).

[5] I. A. Chen, S.-W. Park, G. Chen, C. Wang, C. Bethea, R. Martini, D. Woolard, "Ultra-broadband wavelength conversion sensor using thermochromic liquid crystals", Proc. of SPIE Vol. 8624, p. 862415-1 (2013).

[6] Laser Beam Propagation through Random Media, chapter 4,5,6,7.

[7] Moene, A.F. Boundary-Layer Meteorology (2003) 107: 635. doi:10.1023/A:1022807617073

[8] Sukanta Basu, "A simple approach for estimating the refractive index structure parameter (Cn2) profile in the atmosphere," Opt. Lett. 40, 4130-4133 (2015)

4.B. Quantum theory of QKD over maritime channels.

II. 1 Summary of the previous report on theoretical progress: We have built and extensively tested a Monte-Carlo light propagation model to study the influence of atmospheric aerosols on the free space maritime photon communications. Results have confirmed that 3.95-micrometer wavelength is significantly superior for the maritime QKD under the influence of the highly dynamic weather conditions. Central to the study of a practical maritime free-space quantum communication scheme is its efficiency and security of the information transmission that have become a very challenging task due to the high loss of photons and varied environmental parameters. One efficient way of increasing the shared information between the senders and receivers is to employ a high-dimensional quantum light state. We have found that the spectro-temporal multi-modes (in a well-defined spatial mode) can accomplish high rate quantum key generation in the cases of scattering, absorption, and scintillation. Our analytical methods and numerical simulations have further confirmed that the QKD schemes based on 3.95-micrometer wavelength photons can serve as a robust and persistent information carrier if the high dimensional spectral-temporal modes are employed. Notably, our research on the scintillation influence has gone beyond the single phase screen approach reported in the last report where we started off from the weak turbulence condition. The new significant progress in the past year has been made on several important issues including the multiple phase screen method and strong scintillation conditions. Our new approach has significantly improved the inaccuracy in the strong scintillation range. We have made extensive numerical simulations and found that, for a given waist size, the average probability always monotonically increases with the wavelength irrespective of changes in propagation distance. But it should be noticed that the behavior induced by the waist size can be very complicated, therefore, the numerical simulations must handle the complexity arising from different waist sizes. For a fixed wavelength and propagation distance, we have shown that the maximum value of probalbility of receiving time modes occurs around the value $w_0 = \frac{3}{4}(\frac{\lambda z}{\pi})^{1/2}$.

Our thereotcial results also showed that high-order Schmidt states give rise to high transmission rate. However, such states are more likely affected by the environmental noises, in particular the states are exposed to a strong turbulent influence.

II.2 The new theoretical research: In addition to the further theoretical work in completing the previous findings, our new theoretical investigation emphasizes the interaction between entangled states and environmental noises. Particularly, we have systematically evaluated and tested the entanglement evolution due to the high-level turbulence by using spectro-temporal modes as our input states. Specifically, we prepare our engineered entangled photon pairs as

$$|\Psi\rangle = \frac{1}{\sqrt{2}}(|f_m\rangle|f_m\rangle + |f_n\rangle|f_n\rangle),$$

where

$$|f_n\rangle = \int d\omega \left(\frac{2}{\sigma_a\sigma_b}\right)^{\frac{1}{4}} (2^n n!\sqrt{\pi})^{-\frac{1}{2}} e^{-\frac{(\omega-\frac{\omega_p}{2})^2}{\sigma_a\sigma_b}} \cdot H_n\left(\sqrt{\frac{2}{\sigma_a\sigma_b}}(\omega-\frac{\omega_p}{2})\right)|\omega\rangle,$$

here $H_n(x)$ is the nth Hermite polynomial of x, σ_a is determined by the coherence time of the pump field and σ_b is determined by the phase matching bandwidth of the SPDC source. For a typical SPDC source, σ_b is on the order of hundreds of MHz to several hundred THz. The spatial modes here are treated as the fundenmental Laguerre-Gaussian modes with the lowest radial and azimuthal indices (i.e., Gaussian beams).

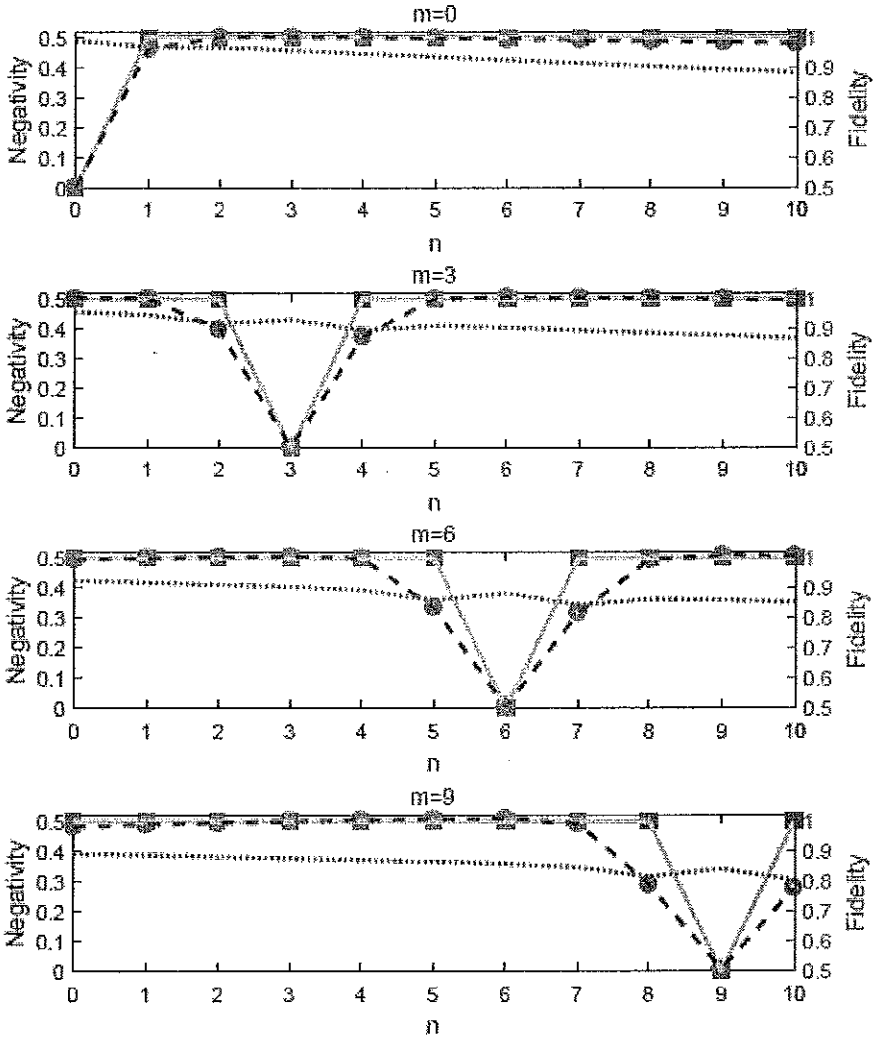

In order to investgate the entanglement evolution of high deminsinonal entangled photon pairs passing though the random media, we choose the log negativity as our entanglement measure. The

above figure is plotted with the parameters $\sigma_a = 10Hz$, $\sigma_b = 80Hz$, $z = 30km$, waist size $w_0 = 14.57cm$. And a strong turbulence condition is assumed $C_n^2 = 2\times10^{-13}m^{-3/2}$ along the propagating path. We keep one photon in a fixed time mode *m* and vary the other photon mode *n* from 0 to 10. The blue squares represent the log negativities of the initial states and the red circles represent the log negativity of the output states at the receiving aperture. Solid lines connect all the squares in every subfigures where dash lines interpolate the circles. The red dot lines plot the fidelities between the initial states and output states. We can see that, when the entangled photons measured by the log negativity can be rather robust even in a strong turbulence regime. More specifically, as indicated in the relation EN(ρ) = log2[2N +1] between the entanglement and negativity, it's easy to see that, when two numbers *m* and *n* are not close, the entanglement will be preserved in propagation through a strong scintillation environment. However, we notice that the fidelity of the entangled states with big *m* or *n* decreases when the states are exposed to the strong turbulence media, this finding confirms our previous observation that "high-order time modes are more likely affected by the environmental noises" in the past progress reports. It is interesting to note that, when two modes are close, interference becomes more intensified, consequently, it leads to strong deoherence of the log negativity. Our new findings will be very useful for selecting entangled photon pairs when the strong scintillation is present.

II.3 Current work: At the moment, we are working on the quantum error correction for the temporal states in the maritime environments. Our major method is to include extra degrees of freedom as a way to recover the affected photonic states. Moreover, it is important to generalize our research to non-Markovian noises where several correlated noises are active at the same time reflecting more realistic situations. In addition, we are working on the transmission with consideration of the curvature of the Earth in the long-distance maritime communication, the optimal protocols will have to be modified to take the curvature into account.

4.III: Experimental Progress on QKD

III. 1 Generation of quantum correlated single photons at 3950 nm

To achieve persistent maritime QKD, we choose to work at 4-micron spectral band for both improved transmittance and suppressed background photon noise. The photon generator and receiver designs are shown in Fig.x.

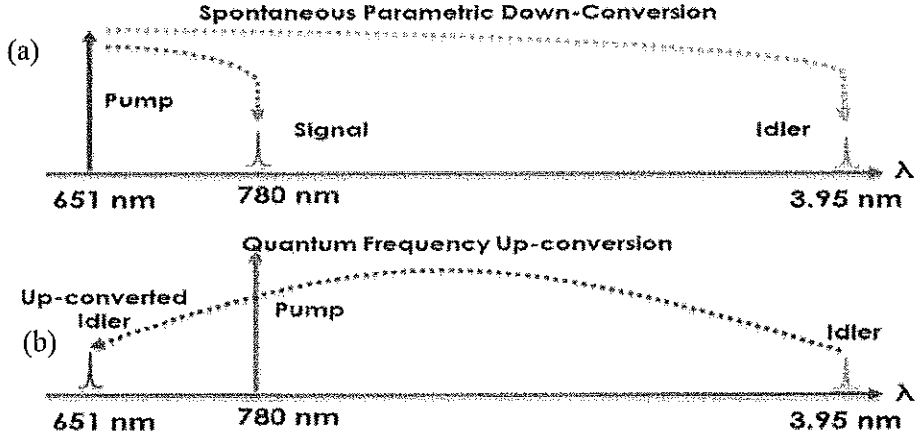

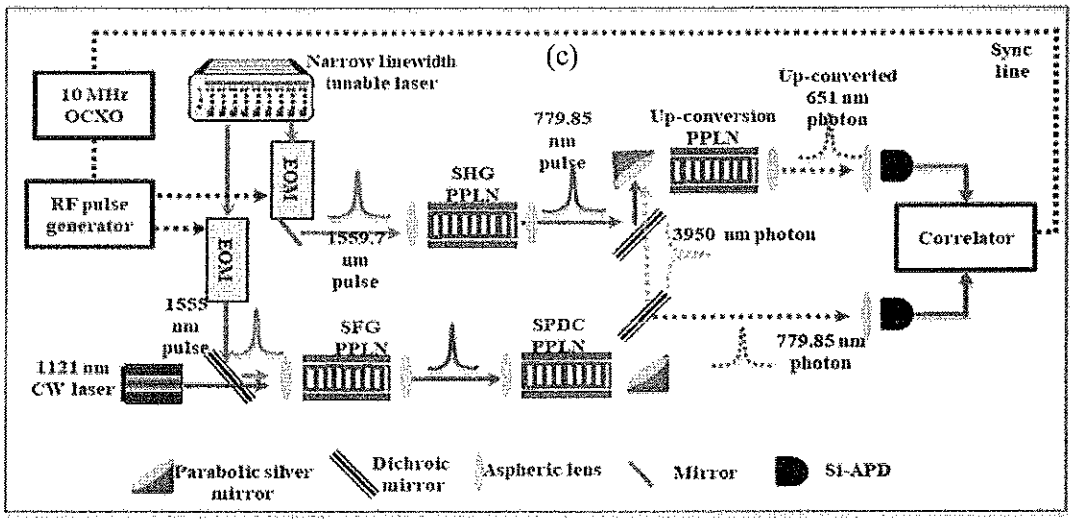

Figure 13: (a) Sketch of SPDC process for the generation of photon pair. (b) Sketch of frequency upconversion process of single photon at 3950 nm to 651 nm. (c) Experimental setup

We develop a scheme for generation and detection of quantum correlated single photons in mid-IR via highly nondegenerate spontaneous parametric down conversion (SPDC) in a Magnesium-doped periodically-poled lithium niobate (MgO:PPLN), as shown in Figure 13.Through SPDC, we generate high purity photon pair with one single photon in the near-infrared and another single photon in the mid-infrared. Single photon in near-infrared is detected directly by a Silicon avalanche photodiode (Si-APD); on the other hand, single photon in mid-infrared is spectral translated into visible wavelength via parametric quantum frequency conversion in another PPLN waveguide and detected by Si-APD.

The experimental setup for generation and detection of quantum correlated photon pair is depicted in Figure 13 (c). The pump pulse is coupled into a 2.2-cm-long PPLN waveguide with about 25% coupling efficiency via an anti-reflection coated aspheric lens. The pump photon at 651.2~nm propagating through the PPLN waveguide will probabilistically decay into a pair of and idler photons signal (651.2 nm =>779.8 nm +3950 nm). An off-axis parabolic silver mirror is used at the output of the SPDC waveguide to achieve achromatic collimation and good coupling for the generated signal and idler photons. Separated by a dichroic beamsplitter, the signal photon which falls within the spectral response of the Silicon avalanche photodiode (Si-APD) detected by using a free running, fiber coupled Si-APD with low-dark-count (<2 Hz), while the idler photons are coupled into second identical PPLN waveguide for frequency up-conversion via SFG with a strong pump pulses at 779.8 nm (779.8 nm +3950 nm =>651.2 nm) and eventually detected by another Si-APD. For signal photon, cascaded bandpass filters centered at 780 nm with 3 nm FWHM bandwidth was used to efficiently reject the residual pump pulse and out of band spontaneous Raman scattering of the pump pulse by more than 140 dB of extinction ratio. However, in-band spontaneous Raman scattering of the pump pulse is not expected to be a dominant noise source due to the large detuning of the pump and signal wavelength.

Considering of the loss of dichroic beamsplitter, parabolic mirror, bandpass filters, free space to fiber coupling efficiency of 30% and quantum efficiency of Si-APD at 780 nm (15%), the total detection efficiency of the 779.8 nm photon is approximately 2%. The signal photon generation probability as a function of pump peak power is depicted in Figure xx, indicating SPDC's linear dependence of the

pump power. The SPDC efficiency is about -106 dB, derived from the slope in figure xx (right).

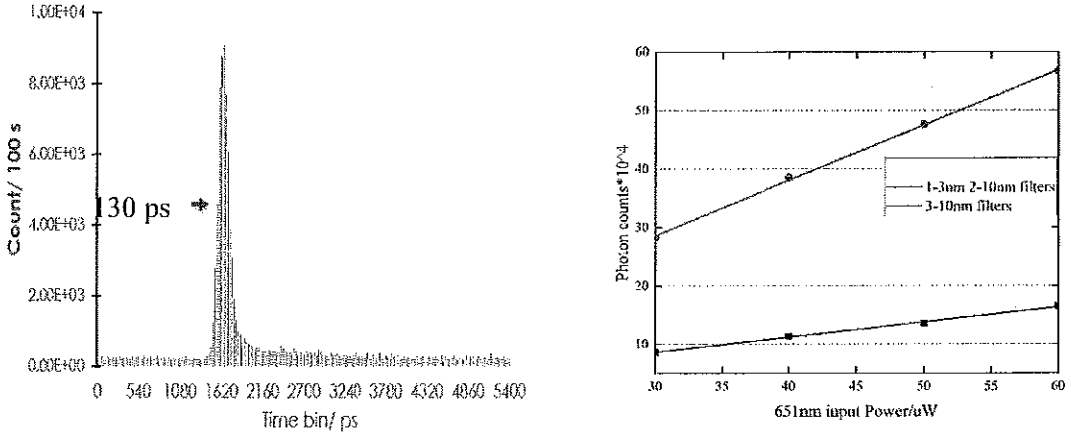

Figure 14, (left) Single photon events histogram of 130 ps FWHM of single photon pulse at 780 nm recorded by single photon detection system over 100 second of integration time.(right) Single photon count for different detection bandwidth plotted against pump power.

We also verify that the presence of noise photon is negligible by measuring the single photon detection outside of the SPDC phase matching bandwidth at 708 nm (10 nm FWHM) and found that the single photon count per detection mode is at least 3 orders of magnitude less than single photon detection inside SPDC phase matching bandwidth. The single photon detection outside of the SPDC phase matching bandwidth is mainly due to the raman scattering of the pump photons.

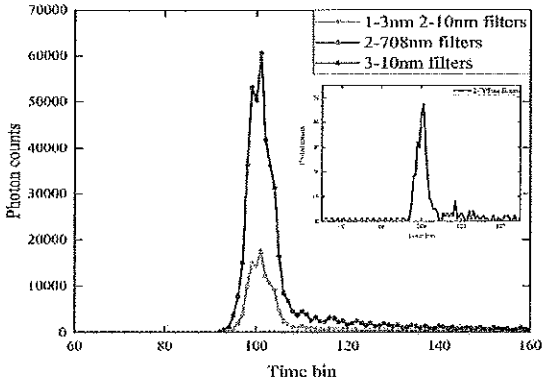

Figure 15, Single photon events histogram of, 130 ps FWHM of single photon pulse at 780 nm with different detection bandwidth and identical pump peak power recorded by single photon detection system over 100 second of integration time. Blue and green color line plot are the single photon detection inside SPDC phase matching bandwidth (inset) histogram of single photon events outside of phase matching bandwidth plotted on enlarged scale

This denotes that the contribution of noise photon due other nonlinear optical interaction such as Raman scattering in the SPDC waveguide does not contribute much to the single photon count and majority of the detection events are attributed to the SPDC process. Figure xx show the histogram of the signal photon arrival time, indicating 130 ps wide (FWHM) nearly transform limited single photon pulse is detected after the filters. As the cascaded filters combined give a spectral bandwidth of 1.4 THz (FWHM), the number of detected time-frequency modes is about 48 for 10 nm bandpass

filter and 16 for 3 nm bandpass filter.

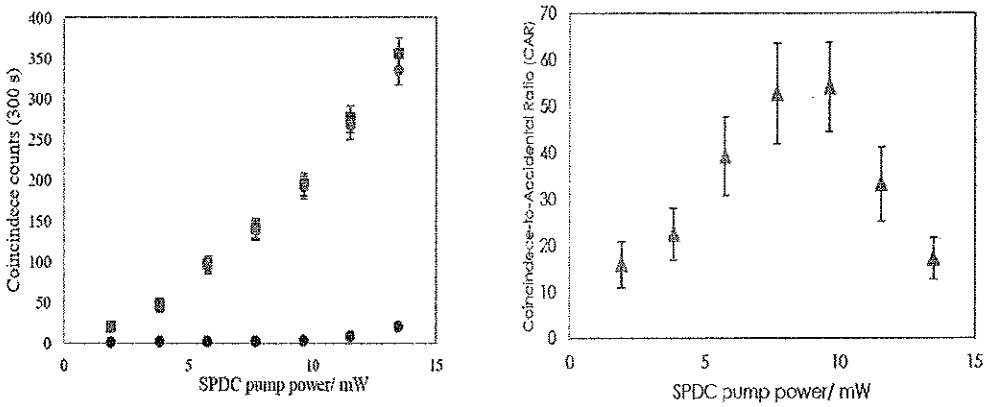

Figure 16: (left) Measured coincidence (Red square), accidental coincidence (black dot), true coincidence (blue dot), integrated in 300 s, plotted as a function of pump peak power. (right) Coincidence-to- accidental coincidence ratio versus pump peak power.

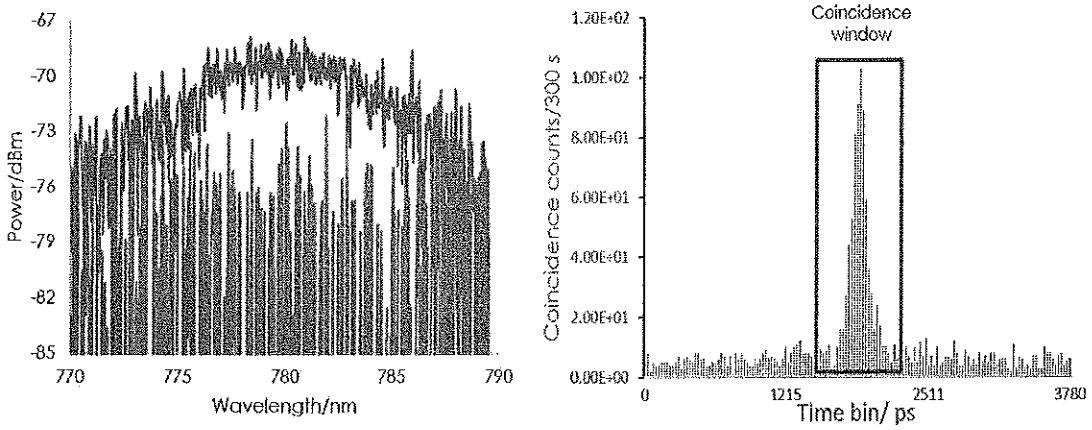

Figure 17: Spectral measurement of fluorescence of the spontaneous parametric down conversion at 780 nm excited by a strong pump pulse at 651 nm, measured by an optical spectrum analyzer after a 10 nm bandpass filter. Blue line is the noise level of the instrument and the red line is the measured fluorescence signal. (b)Typical histogram measurement of the raw coincidence count with integration time of 300 S.

To verify the generation of the quantum correlated photon pair in the wavelengths of interest, we measure the coincidence events of the signal photon (780 nm) and idler photon (3950 nm) detections (via upconversion). A coincidence count is recorded when both Si-APD s detected a photon within the coincidence window, i.e. both Si-APD detects the photon-pair that are born at the same time, while an accidental coincidence count is recorded when both Si-APD s detected a photon outside the coincidence window, which means each Si-APD detects uncorrelated photons induce by two adjacent pump pulse as sketched in figure xx below.

After subtracting the contribution due to the dark count originated from the noise photon in upconversion process, we obtain the coincidence, accidental and true-coincidence counts of the SPDC source. The coincidence, accidental and true-coincidence counts as a function of pump power is depicted in figure 16. The true coincidence which is linearly dependent on pump power is attributed

from the quantum correlated photon pair generated through the SPDC process, while the accidental coincidence arises from simultaneous detection of two uncorrelated photons by each SPAD, thus showing quadratic dependency on pump power. The coincidence, accidental-coincidence counts and net coincidence count as a function of pump peak power for SPDC is showed on figure xx. Coincidence to accidental-coincidence ratio (CAR) is used to determine the quality of quantum correlated photon pair generated via SPDC and verify preservation of quantum correlation in frequency upconversion process. As shown in figure 16, we observe optimum CAR of 54± 7 with pump peak power 7.7 mW. With the CAR of 54, one can generate two photon entangled state with CAR-1/CAR+1 = 96 % of two-photon visibility, thus finding applications in quantum information such as weather proof QKD in mid-IR. The up-conversion waveguide is phased matched at 3950 nm with full-width-half-maximum (FWHM) bandwidth of ~ 6 nm, which intrinsically filters out the undesirable background photons outside the signal band. As shown in figure xx. we achieve coincidence-to-accidental ratio (CAR) of 54±7 with spectral brightness of 4.4 x 10^2 pair/s/nm/mW and photon-pair production rate per pulse of ~0.008.

III. 2 Frequency up-conversion detection of single photons at 3950 nm:

We characterize the absolute quantum up conversion efficiency at single photon level using the correlated photon pair that generated form the aforementioned SPDC waveguide. The idler 3950~nm photons are guided through a bandpass filter (center wavelength =3.95, FWHM = 90 nm) to reject the out of band noise photon in mid-IR wavelength. Then, the idler photon are combined with the pump pulses at 779.8~nm using a dichroic mirror and coupled into up-conversion PPLN waveguide. We placed a set of cascaded optical bandpass filters (center wavelength =650 nm, FWHM = 10 nm) into the path of upconverted photon to reject the pump pulse by extinction ratio of more than 160 dB. Due to the high peak power of the up-conversion pump pulse, it is critical to suppress the up-conversion pump pulse and pump-induced raman noise photon. Inevitably, the in-band raman noise photon will pass through the filer and contributes to noise count of up-conversion detection scheme. The dark count probability and internal conversion efficiency of the mid-IR single photon as a function of pump pulse peak power is depicted in figure xx.

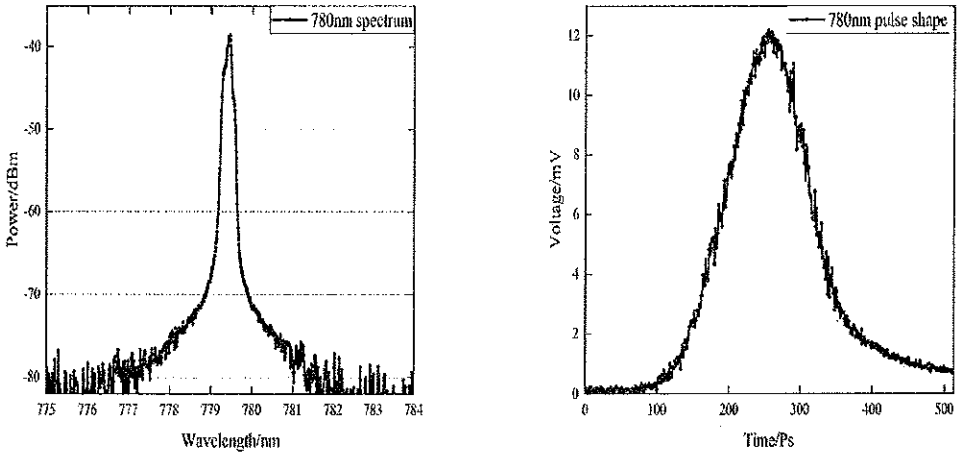

Figure 18, (left) Spectral measurement (right) Time domain measurement of the 10 Mhz repetition rate, 130 ps FWHM, Up-conversion pump pulse at 779.8 nm

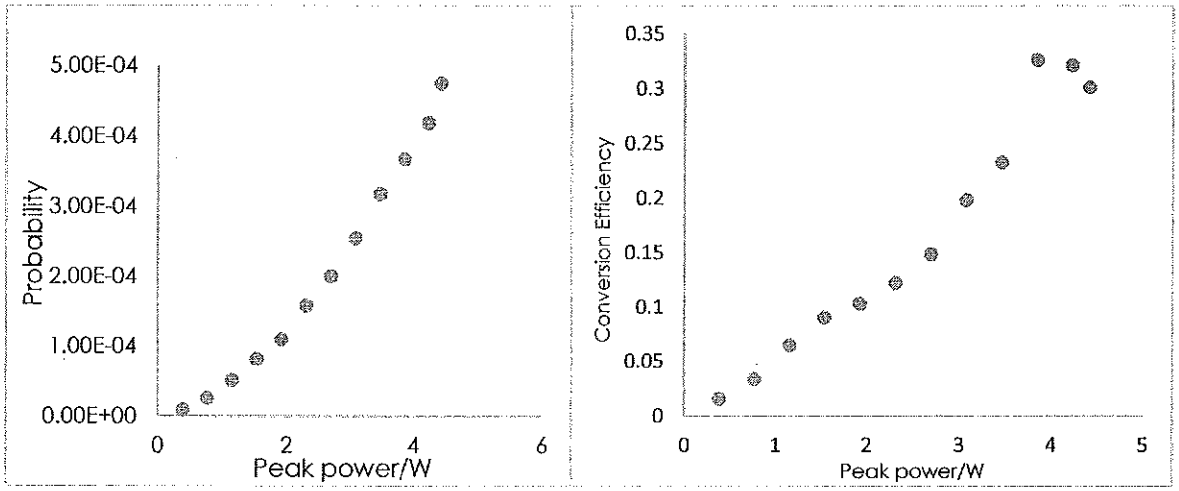

Figure 19(a): noise count probability of the upconversion photon as a function power pump peak power (b) Internal conversion efficiency of the up-conversion waveguide for 130 ps FWHM single photon pulse at 3950 nm

The upconversion efficiency was calculated by the dividing the number of single photon detection after dark count subtraction with respect to the linear loss, quantum efficiency of the SPAD and number of correlated signal photons (780 nm) detected over the same integration period. The highest conversion efficiency of the waveguide is around 32%, reached at the peak power of 3.8 W and reducing beyond this point. We attributed this to partial back conversion of the 651 nm photon into 3950 nm. Taking into account the coupling losses, up-conversion efficiency (32%), and quantum efficiency (25%) of the Si-APD, the total detection efficiency of the 3950~nm single photons is approximately 0.122%. At the 32% up-conversion efficiency, the raw background-photon count induced by the pump is 6.8×10^{-3} per pulse. This can be lowered substantially to 7.4×10^{-6} per pulse by reducing the number of photon detection modes to 1, which will then enable quantum key generation with high speed and low bit error rate. Maintained at 62.2±0.1° Celsius, the up-conversion waveguide is phased matched at 3950 nm with full-width-half-maximum (FWHM) bandwidth 6~nm as shown in figure xx, which is characterized via sum frequency generation by using classical 3950 nm light pulse with identical transform limited properties. The phase matching wavelength can be tuned by controlling the temperature of the WG within the transparency window of lithium niobate which covered beyond 5 um. Phase matching condition of the up-conversion waveguide intrinsically filters out the undesirable background photons outside the signal band which is extremely useful for quantum key distribution in noisy environment. Furthermore, by operating at the edge of phase matching bandwidth using short up-conversion pump pulse in the nonlinear waveguide, the single photons in desirable temporal mode can be selectively up-converted among noise photons which are overlapped in spectral and time domain.

As every detection will be counted as the raw key in quantum key distribution, we characterize the effect of number of detection modes on the total noise count from the up-conversion detection. As predicted, the number of noise count decreased with reduced detection modes. To minimize the detection modes and up-convert the single photon in the desired modes, we will use much narrower (few picosecond) pulses combined with QOAWG technique in our subsequent experiments in near future.

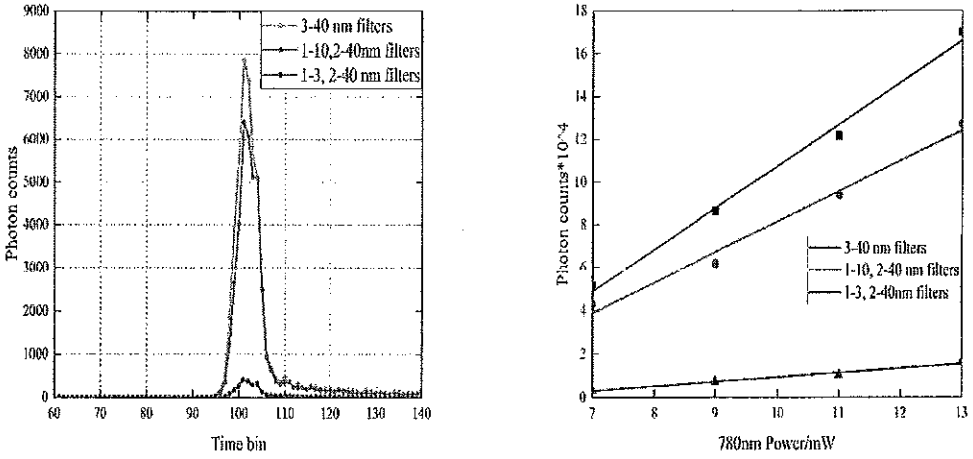

Figure 20: (left) Histogram noise photon detection for 192 (green), 48 (red) and 16 (blue) time-frequency detection modes with integration time of 100 S. (b) Noise photon counts obtained over integration time of 100 S plotted as a function of pump power 48 (black) and 16 (red) time-frequency detection modes. (right) Single photon count for 192 (black), 48 (red) and 16 (blue) time-frequency detection modes plotted against pump power.

We used a 10Mhz repetition rate, 5 ps FWHM of single photon pulse at 780 nm to determine the time jitter of the single photon and coincidence detection system. The timing resolution of the system in determined to be about 81 ps (3 time bins). Thus, to resolve the temporal mode and carry out dispersion measurement in maritime environment, time delay measurement to obtain the convolution of the up-conversion pump pulse at 780 nm with 3950 nm pulse is necessary.

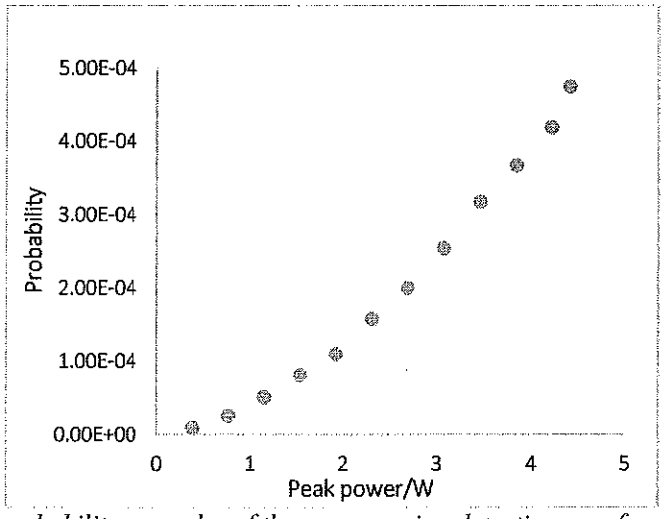

Figure 21: Noise count probability per pulse of the upconversion detection as a function power pump peak power, measured at 300 K in laboratory environment.

To compare the noise count induced by maritime environment, we have measured the noise count probability for 48 detection modes at 300 K in laboratory as the reference. The noise included the

background noise from the laboratory environment, noise originated in the up-conversion waveguide and the raman scattering of the pump pulse. Direct measure of background maritime environment for multiple detection modes at different times over a single day is planned.

III.3 Noise rejection by mode-selective upconversion detection

To deploy persistent Maritime Quantum key distribution, noise photon counts--which can arise from the, multi photon effect, ambient emission and intrinsic dark counts of the APD itself--need to be aggressively suppressed, so that the information carrying single photon can be distinguishable from the noise. To this end, we develop mode-selective up-conversion to enhance the signal-to-noise-ratio of the single photon detection for challenging Maritime environment. Previously, we have shown that by using instead broadband pump pulses whose spectral width is comparable to the phase matching bandwidth, interesting phenomena can occur where only photons in a single time-frequency mode are converted efficiently but the photons in all other modes, including those spanning the exact same spectrum and time of arrival, are converted with much lower efficiency. We utilized this effect to significantly enhance the signal-to-noise ratio for single-photon detection where a weak signal in a single mode is swamped by strong broadband noise randomly distributed in many modes. Here we demonstrate the substantial advantage of how such mode-selective up-conversion compared to direct single photon detection. For proof of principle, we use 1555.7 nm signal pulses and a periodically poled lithium niobate (PPLN) waveguide for the up-conversion. By approaching the phase matching bandwidth of the PPLN waveguide using picosecond optical pulses, we show that only photons in a single spatiotemporal mode, similar to the pump pulse shape in this case, are converted efficiently while background noise photons in all other modes are rejected. Thereby exhibiting significantly enhanced measurement SNR compared to direct detection using an InGaAs-APD.

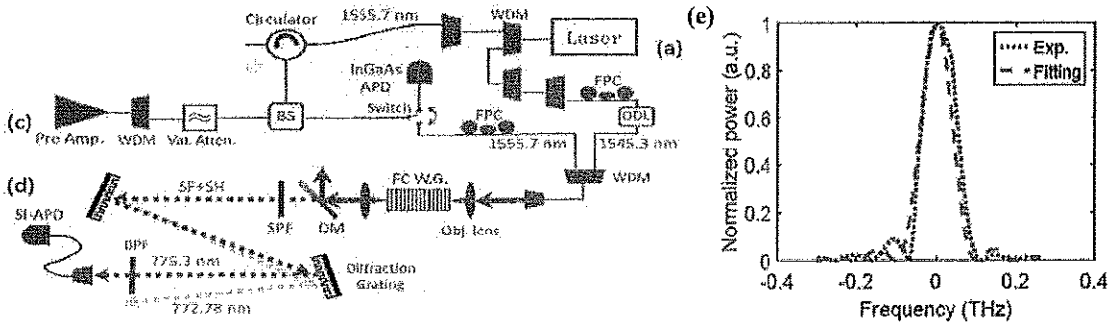

Figure 16 (a) creation of picoseconds pulses (c) generation of broadband noise. (d) mode selective up-conversion system followed by a Si-APD. BS: beam splitter, DM: dichroic mirror, SPF: short pass filter, BPF: band pass filter. (e) Phase matching profile (bandwidth ~ 90 GHz) of the PPLN waveguide, plotted against the frequency offset from 1550.6 nm.

A proof of principle experimental setup for noise mitigation capability of mode-selective up-conversion detection is shown in Fig. 16 (a). Two nearly transform-limited, 6-ps pulses at 1555.7 nm and 1545.3 nm are spectrally carved from a high power femtosecond mode-locked laser by using a set of wavelength-division multiplexing (WDM) filters. To quantify the noise suppression capability of the PMSD, we mix the backscattered photons with broadband noise by using a 50-50 fiber beam splitter, as shown in Fig. 16 (c). The mixed noise and backscattered photons are either sent to a 1 ns gated InGaAS-APD for direct detection, or to the PPLN waveguide for mode-selective up-conversion detection. The backscattered photons and pump are first passed through fiber polarization controllers and then combined in a WDM filter before coupling into a 2-cm PPLN waveguide. An optical delay

line is used to temporally align the pump and the backscattered signal. At the output, the up-converted photons are separated from the pump by using a dichroic mirror followed by a series of noise rejection filter to eliminates any out-of-band noise photon by > 115 dB before detected by using a ultralow noise (dark count: 1.8 Hz) Si-APD.

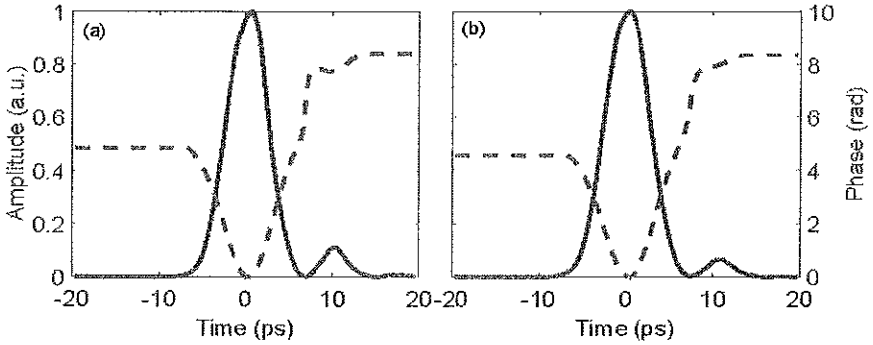

Figure 17. Retrieved pulse shapes by the FROG. (a) and (b) show amplitude and phase profile of generated pulses at 1555.7 nm and 1545.3 nm, respectively.

The pulse shape of the picoseconds probe and up-converting pump pulses carved out from the MLL with WDM filters is measured using a Frequency Resolved Optical Gating (FROG HR--150) with 0.1 ps resolution, Fig. 17. Both pulses are in nearly Gaussian shape with FWHM of 5.8 and 6.1 ps at 1555.7 nm and 1545.3 nm, respectively. A secondary peak appearing 10 ps away from the main peak is due to non-ideal spectral filter shape of the WDM.

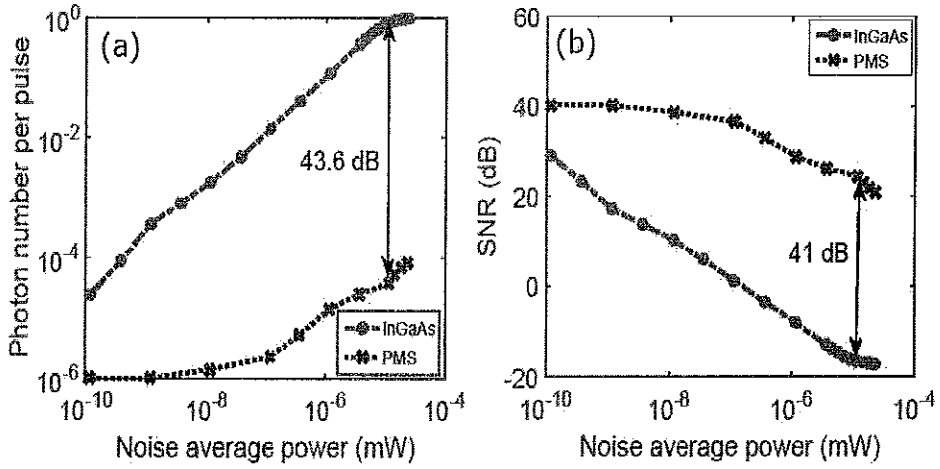

Figure 18. Performance against broadband noise. (a) compares the total detected noise photons by InGaAs detector and PMSD, and (b) compares the corresponding SNR.

We compare the performance of the two detection systems in the presence of the broadband noise, by blocking the backscattered photons from the target and varying the noise power. Figure 18 (a) shows the number of photons per pulse as a function of noise power for the direct detection and the PMSD, respectively. At noise power of 10 nW, the PMSD outperforms the direct detection by as high as 43.6 dB, which implies gigantic advantage for LIDAR applications with strong background light. Considering the overall detection efficiency of 4.5 % for the PMSD and 7.5 % for direct detection with the InGaAs-APD, the PMSD can effectively improve the SNR by as much as 41.4 dB. To measure this, we unblock the backscattered photons from the target while the noise source is

switched off. The measured SNR in the presence of broadband noise is plotted in Fig. 18 (b), confirming the distinct noise rejection advantage of the PMSD. Whereas, 26 dB SNR enhancement is due to reduced time-frequency modes in PMSD compared to direct detection. Additionally, mode-selectivity of the PMSD offers additional 12.5 dB, while another 3 dB enhancement is obtained due to the polarization sensitive frequency up-conversion in PPLN. In conclusion, we observed a 41 dB increase of SNR in single-photon sensitive PMSD from that of direct photon detection using a commercial InGaAs-APD. The noise suppression feature can be useful in mitigating the ambience noise for QKD in Maritime, while the exceptional SNR of single photon detection is crucial for overcoming the high loss cause surrounded by typically foggy Maritime environment.

4.IV Quantum Optical Arbitrary Waveform Generation and Measurement

We have developed a programmable OAWG system based on optical-comb generation and spectral line-by-line pulse shaping, which allows for terahertz-speed processing of photonic signals. The established setup, as shown in Fig. 19, is able to generate high-quality, low-noise sub-picoseconds pulses in arbitrary, custom amplitude and phase profiles for our QKD applications.

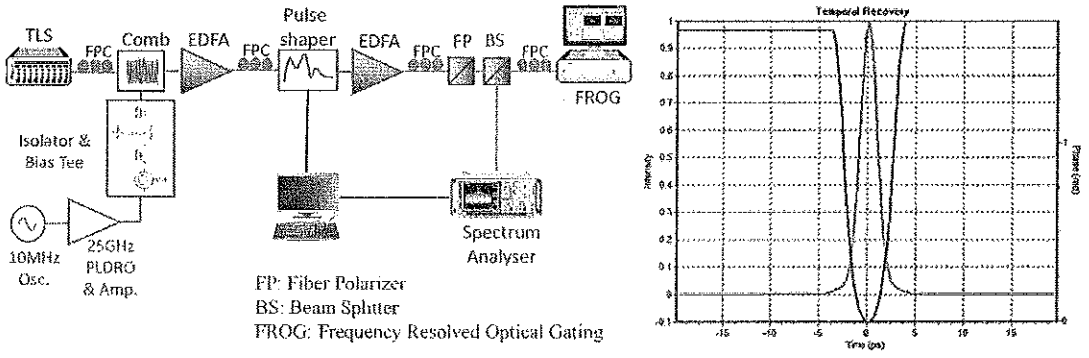

Figure 19: Programmable optical frequency comb generator (OAWG) and an example 2ps transform-limited Gaussian pulse

We have demonstrated up-conversion of overlapping modes with identical spectrum (1555.65 nm + 1563.65 nm-> 779.8 nm). We designed and created a pump, Pump 1, to attain a conversion efficiency of 84% for desirable mode (Signal 1 in Fig. 20) while minimizing the conversion of undesirable mode (Signal 2). The measurement results are shown in Fig. 21(a) where a conversion efficiency of 84% and 6%, respectively, is measured for Signal 1 and Signal 2 when the pump and signals are temporally aligned. A good agreement is seen between the simulation and measurement results without the using of any fitting parameter. Then, we design another pump, Pump 2, to convert Signal 2 as a desirable mode with about 70% efficiency while minimizing the conversion of Signal 1. The results are shown in Fig.21(b), where the conversion efficiency is measured to be 69% and 13% for Signal 2 and 1, respectively.

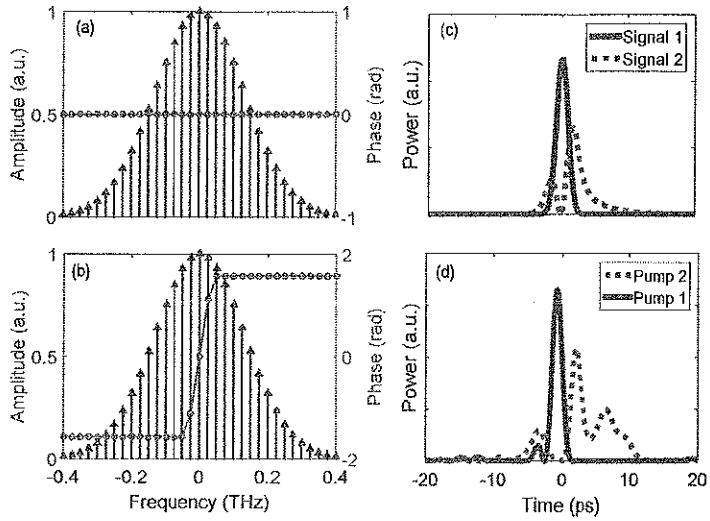

Figure 20: (a) and (b): Spectral profiles of two input signal modes 100% overlapping in the spectrum (spectral width: 220 GHz), but with a π-phase flip across the spectral center. (c): Temporal profiles of the input signals, showing a temporal overlap > 60%. (d): Temporal profiles of the optimized pump pules to selectively convert signal 1 and 2, respectively.

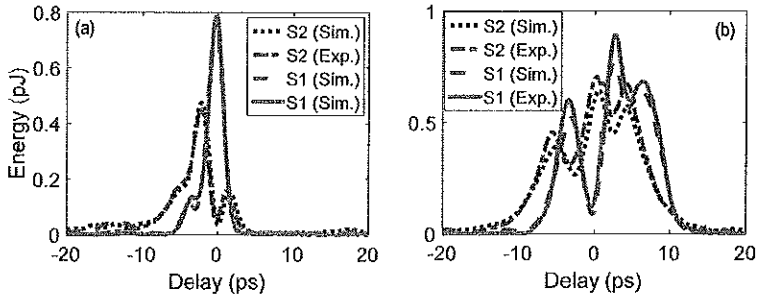

Figure 21: (a) compares the measured and simulated sum-frequency power for both signal modes when they are relatively delayed from the converting pump pulses whose phase and amplitude profiles are optimized for selective up-conversion of Signal 1. (b) Plots the same but with the pump optimized for Signal 2.

We repeated the experiments for a series of signal modes in similar phase and amplitude profiles but of different spectral widths. The results are summarized in Table. 1. With 84% conversion efficiency, the selectivity for Signal 1 exceeds 8.6 dB for a spectral width of 110 GHz (corresponding to 4 ps in pulse width for Signal 1) and increases to 11.3 dB as the spectral width doubles to 220 GHz. A similar trend is seen for Signal 2. These results confirm that a substantially higher selectivity for the same conversion efficiency is achievable with shorter pump and signal pulses relative to the reciprocal of the phase matching bandwidth.

Table 1: Conversion efficiency and selectivity measured for modes 100% overlapping in spectral domain

Spectral FWHM	Desirable mode					
	Mode 1			Mode 2		
	$Conv_{exp}$ (%)	S_{exp} (dB)	S_{sim} (dB)	$Conv_{exp}$ (%)	S_{exp} (dB)	S_{sim} (dB)
110 GHz	84	8.63	8.70	70	6.50	8.00
147 GHz	83	8.75	8.75	72	6.77	8.50
220 GHz	84	11.3	12.5	69	7.18	8.32

Meanwhile, we have tested up-conversion of single photons (1564 nm + 1554 nm-> 779.5 nm) using sum-frequency generation between a weak signal and a strong pump in the aforementioned PPLN ridge waveguide, as shown in Fig. 22. The pump source is an amplified mode shaped pulse at 1554 nm and the single photon is an attenuated signal pulse (of identical shape as Signal 1 in Fig. 12(c) but twice longer) at 1564 nm. The up-converted single photon was then collected into a fiber coupled, and measured by low noise silicon single photon detector e.g., 1.8 Hz in the free-running mode. We counted the total background photons in the sum-frequency band for a 6.8-ps pump pulse similar to the one shown in Fig. 12(d). The pump peak power of the current setup is limited to about 700 mW, which gives 40% conversion efficiency for the desirable signal mode. The total detection efficiency of our system is measured to be 2.7%, which includes the transmission loss of the filters, the free-space to fiber coupling loss, and the APD's quantum efficiency. The raw noise photon counting is 5.52×10^{-7} per pump pulse, which, after taking into account the loss, amounts to $(2.05\pm0.0061)\times10^{-5}$ per pulse. This number can be further reduced to 0.55×10^{-5} per pulse by reducing the number of detected SF modes to one. To demonstrate the operation of the present QPMS at a single-photon level, we attenuate the signal to various photon number per pulse and count the up-converted sum-frequency photons.

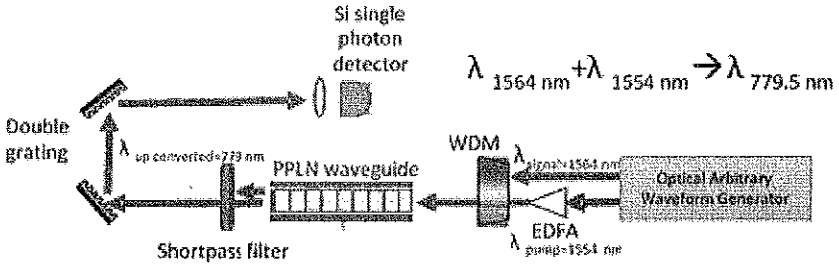

Figure 14: Experiment setup for single-photon detection at 1564 nm via frequency upconversion